

# Chapter 18

## Hydro-mechanical Coupled PFC2D Modelling of Fluid Injection Induced Seismicity and Fault Reactivation



Jeoung Seok Yoon, Arno Zang, Hannes Hofmann, and Ove Stephansson

**Abstract** Many geo-engineering applications, such as unconventional hydrocarbon production, geothermal energy exploitation, or wastewater disposal, require fluid to be injected into the subsurface, and often induces earthquakes. The magnitudes of these fluid-injection induced earthquakes are relatively low – usually  $M < 5$  – compared to natural tectonic earthquakes. However, the hypocenters of these earthquakes locate at shallow depth, and therefore the impacts to the surface structures are not negligible. It became important to understand the physical mechanisms of the fluid injection induced earthquakes, and to develop a reliable numerical simulation tools that can capture the relevant physics and be applied in real engineering applications. In this Chapter, we present numerical simulation of fluid injection in a fractured rock mass using the hydro-mechanically coupled PFC2D modelling. We present two different modelling cases and investigate spatial and temporal evolution of the seismic events induced by fluid injection in a fractured rock mass subjected to an anisotropic stress field. From the modelling of hydraulic stimulation of a fractured rock mass, the results show that the magnitudes of the seismic events generated under a higher stress magnitude and a higher level of stress anisotropy condition are of larger magnitude, and therefore the b-values from the magnitude-frequency distribution is lower. From the modelling of fluid injection near to a fault zone, the results confirm that the magnitudes associated with fault slip tend to be larger in case when the fault zone acts like a fluid flow barrier by generation of large overpressure zone. The obtained results from the two modelling cases are consistent with the laboratory findings and show similarities to the observations in the fields.

---

Ove Stephansson died before publication of this work was completed.

---

J. S. Yoon (✉)  
DynaFrax UG, Potsdam, Germany  
e-mail: [jsyoon@gfz-potsdam.de](mailto:jsyoon@gfz-potsdam.de)

A. Zang · H. Hofmann · O. Stephansson  
Helmholtz Centre Potsdam GFZ German Research Centre for Geosciences, Potsdam, Germany  
e-mail: [arno.zang@gfz-potsdam.de](mailto:arno.zang@gfz-potsdam.de); [hannes.hofmann@gfz-potsdam.de](mailto:hannes.hofmann@gfz-potsdam.de)

**Keywords** Fluid injection induced seismicity · Fault reactivation · Hydraulic stimulation · Hydro-mechanical coupled modelling

## 18.1 Introduction

This chapter presents an application of Particle Flow Code 2D (PFC2D) to a simulation of fluid injection induced fault reactivation. There has been a number of observations in the fields where a large amount of fluid injection caused damaging earthquakes (Zang et al. 2014). The common understanding for such phenomena is that the fluid pressure lowers the normal stress acting on a fault plane and causes fault instability. However, this theory may only apply to a case where the fluid is injected directly on the fault plane, and fails to explain the mechanism of fault reactivation by a distant fluid injection.

Yang et al. (2017) explains that a reactivation of a distant fault by fluid injection is more plausibly explained by the theory of poro-elastic stress triggering, where fluid injection can directly perturb the solid matrix stresses in the surrounding media and bring faults with preferred orientations closer to failure. Goebel et al. (2017) observed that a fault located >40 km from the injection can be reactivated by the poro-elastic stress triggering.

There is also a discussion that a seismic magnitude evolving at a fault zone associated with fluid injection may vary depending on the hydraulic properties (fluid barrier vs. fluid conduit, Caine et al. 1996) and maturity of the fault (Jeanne et al. 2014).

In this chapter we present two modelling cases of fluid injection and fault reactivation. From the first modelling case, we investigate how a fractured reservoir at depth subjected to an anisotropic stress field could respond to a fluid injection, and how the induced seismic events evolve with time and space. From the second modelling case, we investigate how faults possessing different hydraulic characteristics, and therefore different maturity, can be reactivated by a distant fluid injection.

## 18.2 Model Description

The first model is a fractured rock mass intersected by a fault. The model contains two sets of fractures with length of 200 m, but different orientation: +30 and -30 degrees from the model horizontal axis. The fault is also inclined by 30 degrees and has a length of 2 km (Fig. 18.1). The fractured reservoir is subjected to an anisotropic stress field. The minimum horizontal stress,  $S_{h, min}$  is 30 MPa. In one case, the maximum horizontal stress,  $S_{H, max}$  is 45 MPa which results in a stress ratio of 1.5. In the other case,  $S_{H, max}$  is 60 MPa, and the resulting stress ratio is 2.

The fractures and the fault are represented by smooth joints. The mechanical properties, e.g. tensile strength, cohesion, friction angle, dilation angle, friction coefficients are set the same for the fractures and the fault, for simplicity. Table 18.1 lists the mechanical properties.

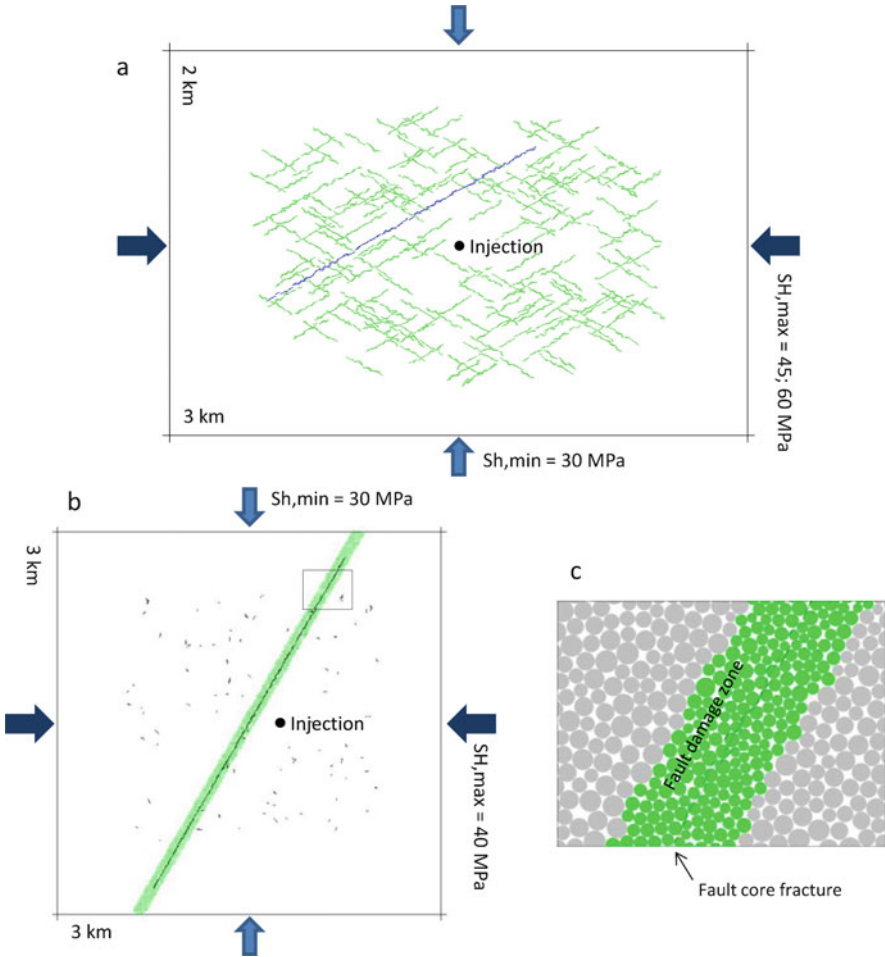


**Fig. 18.1** (a) Model 1: Rock mass containing fractures and a fault that are both represented by smooth joints, and subjected to anisotropic stress field, (b) Model 2: Rock mass containing a fault zone represented by a fault damage zone represented by parallel bonds and fault core fractures modelled by smooth joints and subjected to an anisotropic stress field

**Table 18.1** Mechanical properties of the fractures and the fault in Model 1

Property	Value (Unit)
Normal stiffness, $K_n$	300e6 (Pa/m)
Shear stiffness, $K_s$	50e6 (Pa/m)
Tensile strength, $\sigma_t$	1 (MPa)
Cohesion, $c$	5 (MPa)
Friction angle, $\phi$	30 (deg.)
Dilation angle, $\psi$	5 (deg.)
Friction coefficient, $\mu$	0.6

**Table 18.2** Mechanical properties of the fault damage zone and the fault core fractures

	Property	Value (Unit)
Fault damage zone	Young’s modulus	40 (GPa)
	Tensile strength, $\sigma_t$	2 (MPa)
	Cohesion, $c$	5 (MPa)
	Friction angle, $\phi$	30 (deg.)
Fault core fracture	Normal stiffness, $K_n$	30e9 (Pa/m)
	Shear stiffness, $K_s$	2e9 (Pa/m)
	Tensile strength, $\sigma_t$	0.1 (MPa)
	Cohesion, $c$	0.5 (MPa)
	Friction angle, $\phi$	30 (deg.)
	Dilation angle, $\psi$	3 (deg.)
	Friction coefficient, $\mu$	0.5

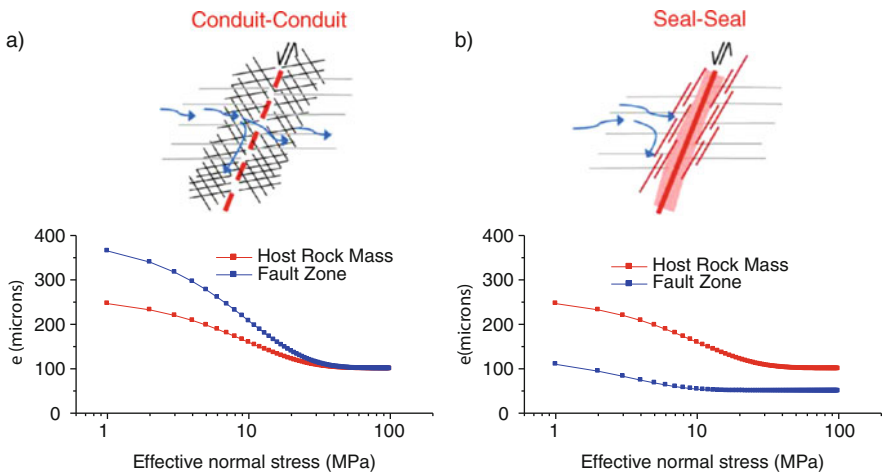


**Fig. 18.2** Schematics of two different fault models: (a) fluid conduit-conduit model and (b) fluid seal-seal model (Rohmer et al. 2015). The bottom figures show the hydraulic aperture and normal stress relations assigned to the contacts in the rock mass part and in the fault zone

The second model is shown in Fig. 18.1b which represents a 10 m thick horizontal layer at depth and subjected to an anisotropic stress field with  $S_{H, max}$  and  $S_{h, min}$  of 40 MPa and 30 MPa, respectively. An inclined fault zone is modelled as a combination of damage zone and core fractures. The damage zone is represented by smaller particles that are bonded with stiffness and strength lower than those in the host rock mass. The damage zone is 100 m wide and the fault core fractures are represented by the smooth joint model of which the properties are listed in Table 18.2.

Hydraulic behavior of the fault zone is modelled differently from the host rock mass by assigning different normal stress vs. hydraulic aperture relation to the contacts that are in the damage zone and the host rock mass as shown in Fig. 18.2.

The first one is called fluid conduit-conduit model, and the second one is called fluid seal-seal model (Rohmer et al. 2015).

### 18.3 Model Results

#### 18.3.1 Hydraulic Stimulation of a Fractured Reservoir and Fault Reactivation: Model 1

Fluid injection with changing rates over time (20, 25 and 30 l/s maintained for 2 h for each rate step) is applied at the injection point at the model center. The total volume of injection is 540 m<sup>3</sup>. Figure 18.3a shows the temporal and spatial distribution of the seismic events. The event symbol is colored according to the occurrence time, and

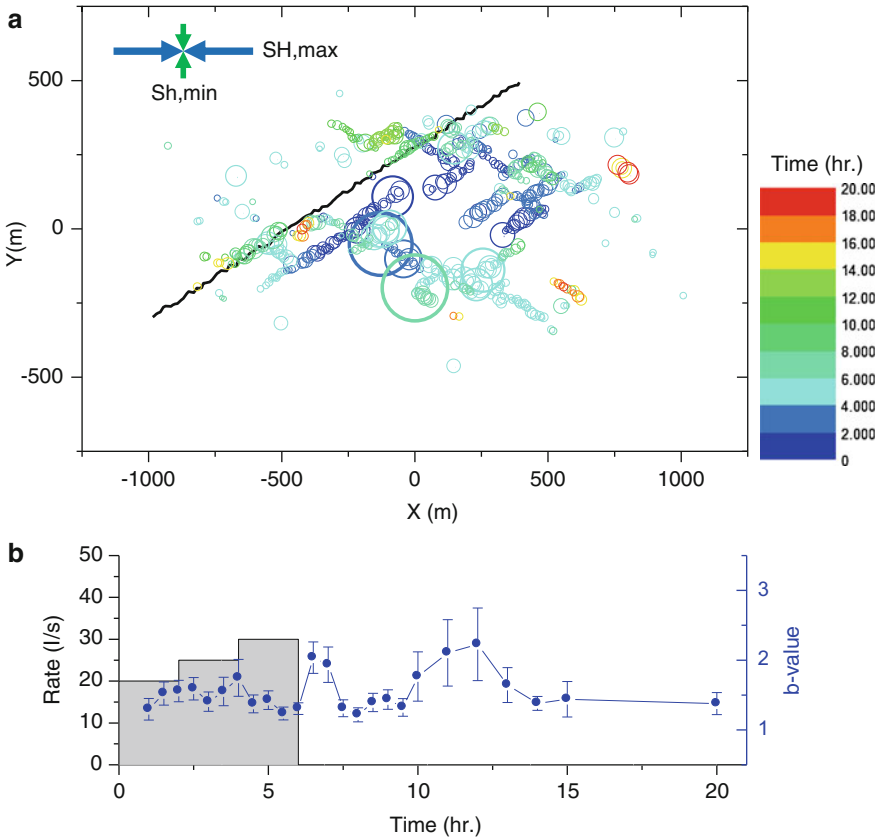


**Fig. 18.3** (a) Temporal and spatial distribution of the induced seismic events and (b) temporal changes in the b-value of the seismic events in the fractured reservoir subjected to lower stress anisotropy condition

the size of the symbol is proportional to the stress drop ( $\Delta\sigma$ ) of the seismic event which is calculated by the following equation (Lay and Wallece 1995):

$$\Delta\sigma = \frac{7M_0}{16R^3} \quad (18.1)$$

where,  $M_0$  is the seismic moment (Nm) of the event and  $R$  is the source radius (m), which is calculated by the acoustic emission moment tensor modelling in PFC2D v4 (Hazzard and Young 2000, 2002; Hazzard et al. 2000; Yoon et al. 2014).

Magnitude-frequency distribution of the seismic events is analyzed and the slope of the distribution is calculated by the maximum likelihood method (Bender 1983) using Equation (18.2). The slope of the distribution is called b-value (Gutenberg and Richter 1944).

$$b = \frac{0.434}{(M_{avg} - M_c)} \quad (18.2)$$

where,  $M_{avg}$  is the average of the seismicity magnitudes within a given space and time interval, and  $M_c$  is the magnitude of completeness within a given space and time interval.

The temporal changes in the b-value of the seismicity under lower anisotropy stress condition are plotted in Fig. 18.3b together with the injection rate history. During the injection, the b-value is stable. The seismic events induced during the injection are the blue events, which are mostly aligned along the fractures in the right part of the fault. The b-value shows slight decrease at the time of injection rate increase. The b-value starts to fluctuate with involvement of more green events which are located closer to the fault. Two sharp drops of the b-value are associated with the seismic events that occurred near to and along the fault trace. It can be interpreted that the seismic events occurring near the fault trigger the movement of the fault and the fault movement induces local stress changes. Those parts in the reservoir with high fracture density and structural complexity could undergo sudden stress changes and generate seismicity clusters which develop into a few larger magnitude seismic events. This mechanism may explain the sudden drop of the b-value.

Under the higher anisotropy stress condition, more seismic events appear with large stress drop as shown in Fig. 18.4a. Contrary to the first case, more seismic events appear during the injection and at the left part of the fault. Same as in the first case, the b-value slightly decreases at the time of injection rate increase. However, the b-value changes more rapidly during the injection and records the first sharp drop at 5 h. This is due to the large seismic events along the fractures at the right part of the fault which was not pronounced in the lower stress anisotropy condition. The b-value shows another sharp drop at approximately 8 h. This b-value drop is

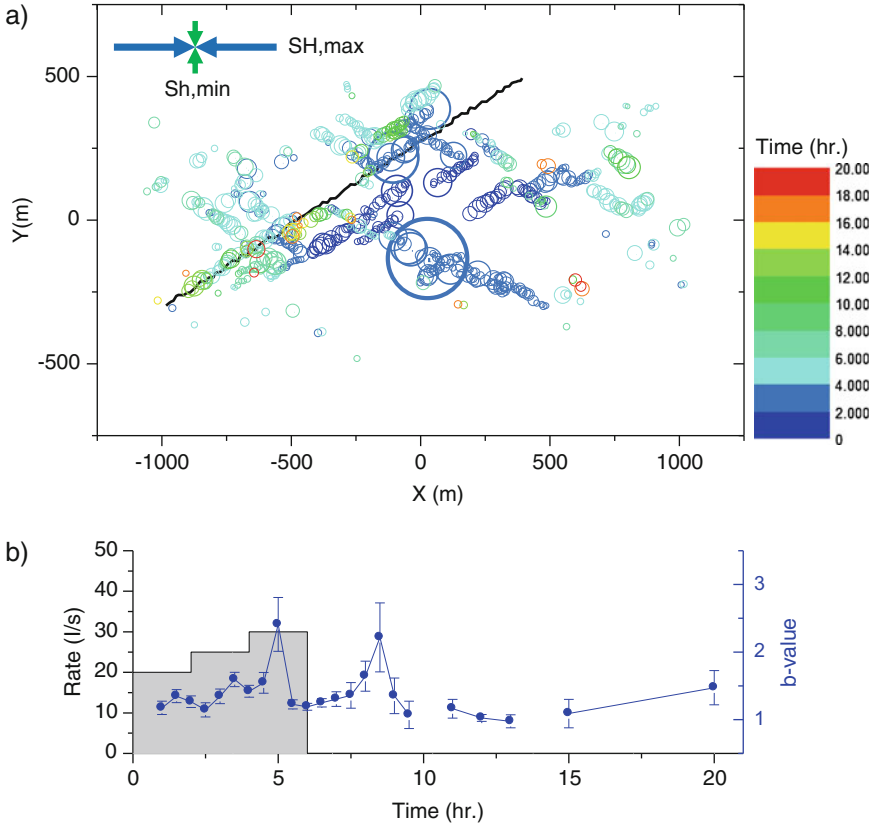


**Fig. 18.4** (a) Temporal and spatial distribution of the induced seismic events and (b) temporal changes in the b-value of the seismic events in the fractured reservoir subjected to higher stress anisotropy condition

attributed to the seismic events that are located along the fault trace which bring the fault to dynamic slip and cause more seismic events around the fault with higher magnitudes.

The magnitude-frequency distributions of all the seismic events are plotted in Fig. 18.5. The b-values are computed using the maximum likelihood method using Eq. 18.2. The magnitude of completeness,  $M_c = -0.3$ . The b-value of the seismic events generated under the higher stress anisotropy condition is lower than that under the lower stress anisotropy condition. This result is consistent with the results of laboratory experiments by Amitrano (2003) where the b-value associated with rock failure under a higher confining stress is usually lower than that under a lower confining stress.

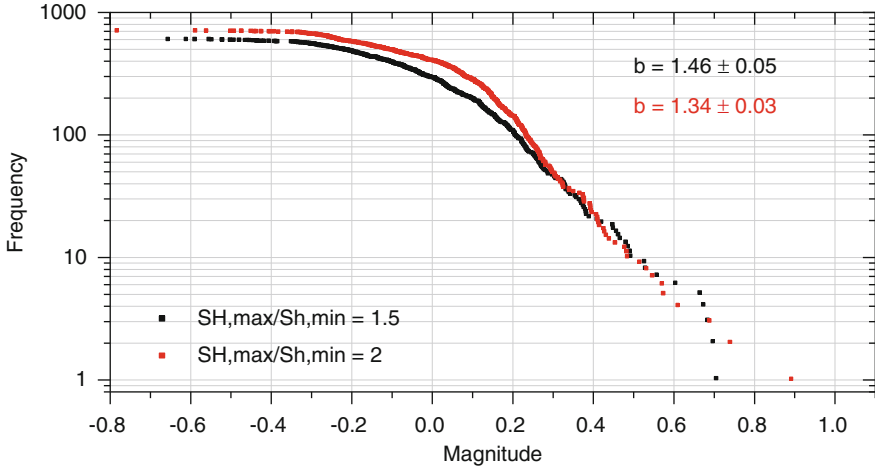


**Fig. 18.5** Magnitude-frequency distribution of the seismic events in the (a) fluid conduit-conduit model and (b) fluid seal-seal model, and the b-values (mean  $\pm$  standard deviation)

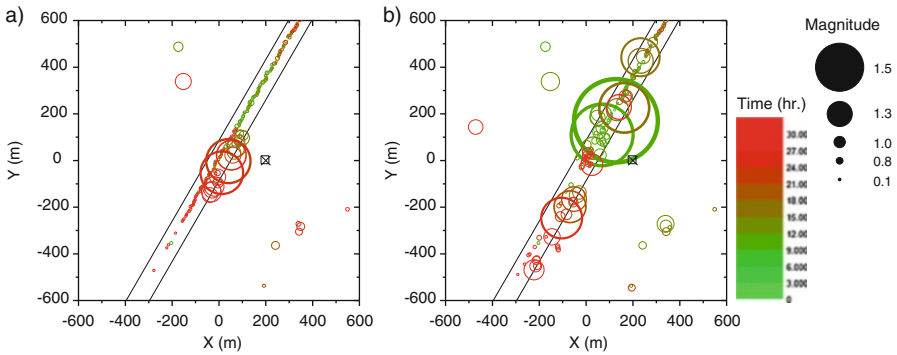


**Fig. 18.6** Temporal and spatial distributions of the induced seismic events in the (a) fluid conduit-conduit model and (b) fluid seal-seal model. The size of the symbol scales with the seismic radiated energy,  $E_s$ , and the symbol colour corresponds to the time of occurrence

### 18.3.2 Fluid Injection Induced Fault Reactivation: Effect of Fault Zone Permeability: Model 2

Fluid injection with changing rates over time (30, 40 and 50 l/s maintained for 10 h for each rate step) is applied at 200 m distance from the fault zone (Fig. 18.1b). The total volume of injection is 4320 m<sup>3</sup>.

Figure 18.6 shows the temporal and spatial distributions of the induced seismic events. The size of the symbol is proportional to the radiated seismic energy,  $E_s$ , of the seismic event (Gutenberg and Richter 1956) using the following equation:



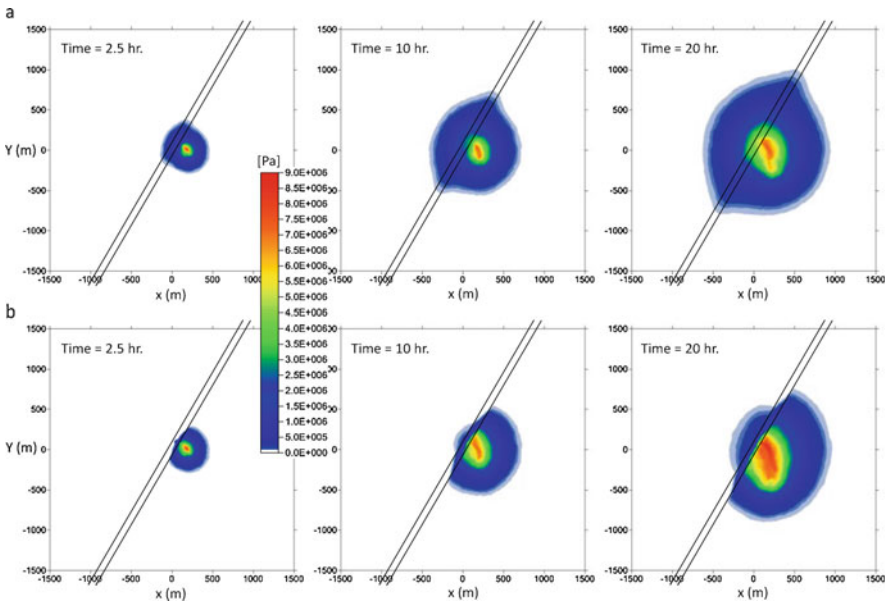
$$\log(E_s) = 4.8 + 1.5M_w \quad (18.3)$$

where,  $M_w$  is the moment magnitude of the seismic event, which is calculated by the acoustic emission moment tensor modelling in PFC2D v4 (Yoon et al. 2014).

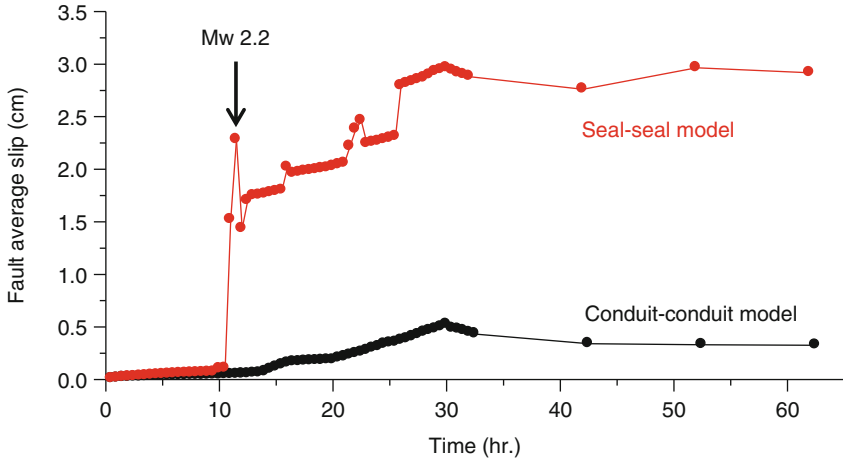
There is a significant difference between the two models. In the fluid conduit-conduit model, the seismic events are of low magnitude, whereas the seismic events in the fluid seal-seal model are of high magnitude. The largest circle represents a seismic event with  $M_w$  2.2. The reason for the difference in the magnitude of the seismicity can be explained in conjunction with the fluid pressure distribution.

Figure 18.7 shows the fluid pressure distribution at three selected times during the injection in the (a) fluid conduit-conduit model and (b) fluid seal-seal model. In the fluid conduit-conduit model the fluid easily migrates into the fault zone and follows the fault zone relatively fast compared to the host rock mass. As fluid migrates along the fault zone, the fluid lowers the effective normal stress acting on the fault core fractures, which then leads to shear failure. This process can be explained by the theory of effective stress.

In the fluid seal-seal model, the injected fluid cannot fully migrate into the fault zone due to the low permeability barrier. Instead, the fluid migrates along the interface between the host rock mass and the fault zone. As a result, a large zone of fluid overpressure builds up at one side of the fault zone. Such large zone of fluid overpressure further pushes the fault zone in addition to the far field in-situ stress field. Therefore, the magnitudes associated with the failure of the fault core fractures



**Fig. 18.7** Spatial distribution of the fluid pressure monitored at different selected times during the fluid injection in the (a) fluid conduit-conduit model and (b) fluid seal-seal model



**Fig. 18.8** Average slip of the fault core fractures induced by fluid injection in the fluid conduit-conduit model (black curve) and in the fluid seal-seal model (red curve). The large spike in the slip curve is associated with the occurrence of  $M_w$  2.2 seismic event

under elevated stress level are larger. This may explain the difference in the magnitudes of the seismic events in the fluid conduit-conduit model and the fluid seal-seal model. Such large zone of high fluid pressure exerts additional effect for inducing seismic events at near and at far field. This effect can be called poro-elastic triggering (Goebel et al. 2017) where the fluid pressure pushing the rock mass and the elastic stress transfer causes additional seismic events that are located at critically stressed fractures.

We used the maximum likelihood method (Bender 1983) to compute the b-value of the magnitude-frequency distribution of the seismic events, and the results are  $b = 1.9$  and  $b = 0.9$  for the fluid conduit-conduit model and the fluid seal-seal model, respectively.

The numerical results showed that the seismic events generated under the higher stress state have larger magnitude, and therefore result in lower b-value (0.9) of the magnitude-frequency distribution which is consistent with the results of the triaxial compression tests by Amitrano (2003). It was found that for all different states of the rock mechanical behavior (linear, non-linear pre-peak, non-linear post-peak, shearing) there is a systematic decrease of the b value with increasing confining pressure. This is also in agreement with earthquake observations by Mori and Abercrombie (1997) who observed a systematic decrease in b-value with increasing depth of earthquakes in California between 1974 and 1996. It is suggested that such depth dependence of the b-value could be due to an increase in confining pressure as depth increases.

We monitored the average slip of the fault core fractures which are presented in Fig. 18.8. Compared to the temporal fault slip change in the fluid conduit-conduit

model, the slip of the fluid seal-seal model shows drastic increase associated with the occurrence of the  $M_w$  2.2 seismic event, which is then followed by a few sharp slip increases. The first large slip increase can be referred to as a main-shock and a few sharp slip increases are the after-shocks. This result demonstrates that an immature fault with a damage zone acting as a fluid flow barrier could have higher potential of seismic hazard.

The permanent slip of the fault core in the fluid conduit-conduit model is larger than the fluid seal-seal model by a factor of six. The result implies that the seismic hazard potential associated with fault reactivation induced by fluid injection can be larger in case when a fluid injection operation is conducted near to a fault with low permeability than in case of a high permeability fault zone.

## 18.4 Discussion

The two fault zone models with different hydraulic properties of the damage zones can be linked to the concept of fault maturity. Perrin et al. (2016) discussed that size of the damage zone is dependent on fault maturity. As a fault ages, net displacement increases which results in enlargement of the outer damage zone and increased connection of the segments in the damage zone, which consequently leads to increased hydraulic connectivity (permeability). Therefore, the fluid conduit-conduit model mimics relatively more mature faults than the fluid seal-seal model.

In a mature fault zone the higher permeability damage zone allows the fluid to move easily into the damage zone and diffuse along the fault zone. This prevents any important pressurization of the fault zone. This process does not allow a rupture with significant seismic magnitude since the overpressure along the fault zone is lower compared to an immature fault zone. Similar results were obtained by Jeanne et al. (2014), where they conducted a series of 2D thermo-hydro-mechanical coupled TOUGH-FLAC simulation of fault reactivation induced by CO<sub>2</sub> injection with different levels of hydro-mechanical heterogeneity.

Figure 18.9 shows the slip distribution of the fault core fractures (smooth joint) with respect to the distance from the fault left tip. The conduit-conduit model indicated by the black curve shows that the slip is more smoothly and evenly distributed along the fault without spikes of large slip. The slip of the fault core in the seal-seal model (red curve) has multiple high slip spikes and is generally on a higher slip level.

The area under the distance-slip curve is calculated by integrating the area from the left tip to the right tip. This quantity provides the slip volume,  $\Delta V_{\text{slip}}$  (m<sup>3</sup>) when multiplied by the fault width which is 10 m in this case (model dimension in the out-of-plane direction). The slip volume is then multiplied by a shear modulus of 30 GPa to estimate the seismic moment  $M_0$ .

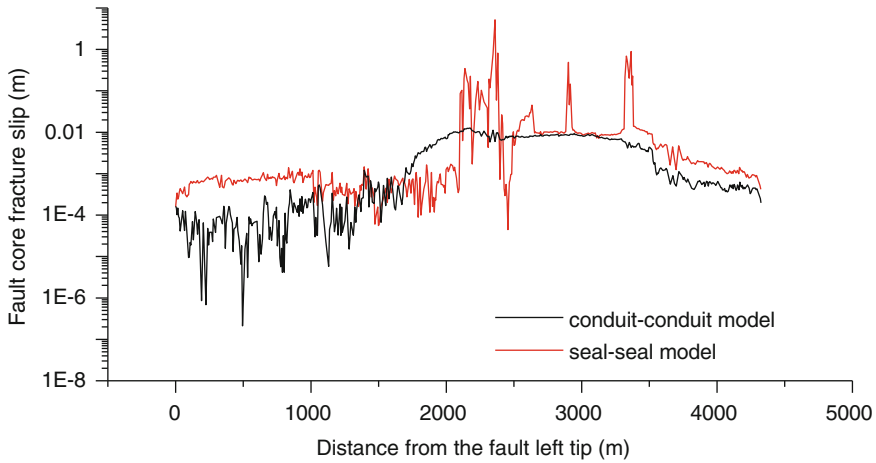


**Fig. 18.9** Distribution of slip of the fault core fractures induced by fluid injection in the fluid conduit-conduit model (black curve) and in the fluid seal-seal model (red curve)

**Table 18.3** Slip volume of the faults, seismic moments and the moment magnitudes of the fault reactivation in the fluid conduit-conduit model and the fluid seal-seal model

Model	Slip volume (m <sup>3</sup> )	Seismic moment, $M_0$	Moment magnitude, $M_w$
Conduit-conduit	141	4.24e12	2.42
Seal-seal	1637	4.91e13	3.13

Another calculation is done using the following equation of McGarr (2014) for estimating the maximum magnitude from a injected fluid volume,  $\Delta V_{inj}$ :

$$M_{0,max} = G\Delta V_{inj} \tag{18.5}$$

The  $M_{0,max}$  serves as an upper bound of the seismic moment induced by fluid injection. The seismic moment and the moment magnitudes estimated by the slip volume of the fault core fractures in the fluid conduit-conduit model and the fluid seal-seal model are presented in Table 18.3. The calculated magnitudes are lower than the magnitude estimated by the equation of McGarr (2014) as shown in Figure 18.10.

### 18.5 Conclusions

By the hydro-mechanical coupled modelling of fluid injection and induced seismicity using PFC2D v4, we investigated the spatial and temporal evolution of the seismic events induced by fluid injection in a fractured rock mass subjected to an anisotropic stress field.

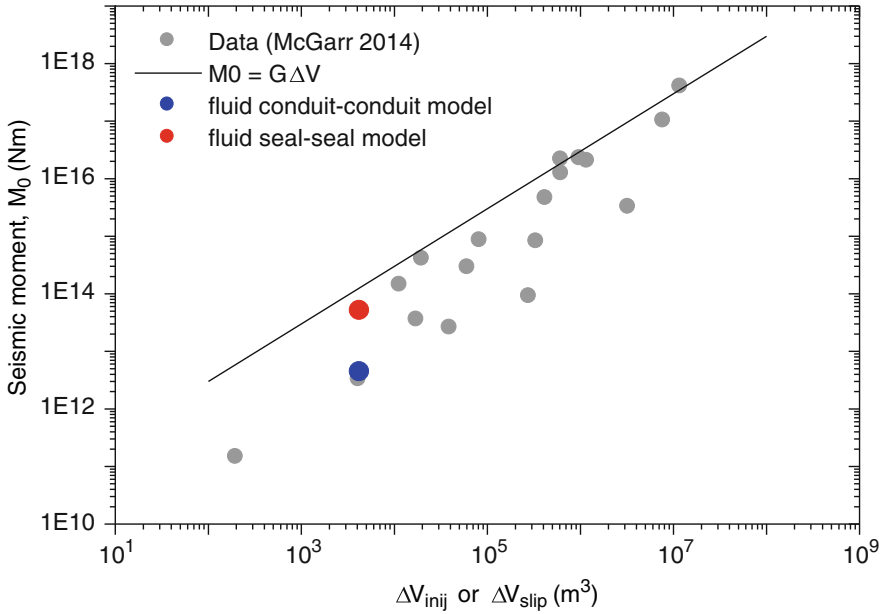


**Fig. 18.10** Maximum seismic moment,  $M_{0,max}$ , as a function of total volume of injected fluid ( $\Delta V_{inj}$ ) and the data from McGarr (2014) and the results of two modelling cases based on the slip volume ( $\Delta V_{slip}$ )

From the modelling of hydraulic stimulation of a fractured rock mass, the results confirmed that the magnitudes of the seismic events generated under a higher stress magnitude and a higher level of stress anisotropy condition are of larger magnitude, and therefore the Gutenberg-Richter b-values from the magnitude-frequency distribution is lower. This result is consistent with the laboratory test results on rock failure and observations from some of the geothermal fields.

From the modelling of fault reactivation induced by fluid injection, the results confirmed that the magnitudes associated with fault slip tend to be larger in case when the fault zone acts like a fluid flow barrier than in the case when the fault zone acts as a fluid flow conduit. The reactivation magnitudes estimated by the fault slip distribution are lower than the maximum magnitude of fault reactivation estimated by the injection volume by McGarr (2014). The results show that the magnitudes of fluid injection induced seismicity are generally larger in case of a fluid injection near to a less permeable fault system at a near-critical stress state than with permeable fault systems, and therefore the induced seismic hazard and risk could be larger.

**Acknowledgements** The author would also like to thank our collaboration partners in the International Collaboration Project on Coupled Fracture Mechanics Modelling. This work is partially supported by the International Consignment Research Project of Korea Institute of Geoscience and Mineral Resources (KIGAM) (project title: Development of particle mechanics based discrete element model simulation workflow for thermo-hydro-mechanical coupled processes) and by the Impulse and Network Fund of the Helmholtz Association e.V. (grant: HE-2017-10, project title: DcubeRoc).

## References

- Amitrano D (2003) Brittle-ductile transition and associated seismicity: experimental and numerical studies and relationship with the  $b$  value. *J Geophys Res* 108(B1):2044
- Bender B (1983) Maximum likelihood estimation of  $b$  values for magnitude grouped data. *Bull Seismol Soc Am* 73:831–851
- Caine JS, Evans JP, Forster CB (1996) Fault zone architecture and permeability structure. *Geology* 24:1025–1028
- Goebel THW, Weingarten M, Chen Y, Haffener J, Brodsky EE (2017) The 2016 Mw5.1 Fairview, Oklahoma earthquakes: evidence for long-range poroelastic triggering at >40 km from fluid disposal well. *EPSL* 472:50–61
- Gutenberg B, Richter C (1944) Frequency of earthquakes in California. *Bull Seismol Soc Am* 34:185–188
- Gutenberg B, Richter C (1956) Earthquake magnitude, intensity, energy and acceleration (second paper). *Bull Seismol Soc Am* 46:105–145
- Hazzard JF, Young RP (2000) Simulating acoustic emissions in bonded-particle models for rock. *Int J Rock Mech Min Sci* 37:867–872
- Hazzard JF, Young RP, Maxwell SC (2000) Micromechanical modeling of cracking and failure in brittle rocks. *J Geophys Res* 105(B7):683–397
- Hazzard JF, Young RP (2002) Moment tensors and micromechanical models. *Tectonophysics* 356:181–197
- Jeanne P, Guglielmi Y, Cappa F, Rinaldi AP, Rutqvist J (2014) The effect of lateral property variations on fault zone reactivation by fluid pressurization: application to CO<sub>2</sub> pressurization effects within major and undetected fault zones. *J Struct Geol* 62:97–108
- Lay T, Wallece TC (1995) Modern global seismology. Academic, San Diego
- McGarr A (2014) Maximum magnitude earthquakes induced by fluid injection. *J Geophys Res Solid Earth* 119. <https://doi.org/10.1001/2013JB010597>
- Mori J, Abercrombie RE (1997) Depth dependence of earthquake frequency-magnitude distributions in California: implications for rupture initiation. *J Geophys Res* 102:15081–15090
- Perrin C, Manighetti I, Ampuero JP, Cappa F, Gaudemer Y (2016) Location of largest earthquake slip and fast rupture controlled by along-strike change in fault structural maturity due to fault growth. *J Geophys Res Solid Earth* 121:3666–3685
- Rohmer J, Nguyen TK, Torabi A (2015) Off-fault shear failure potential enhanced by high-stiff/low-permeable damage zone during fluid injection in porous reservoirs. *Geophys J Int* 202:1566–1580
- Yang HF, Liu Y, Wei M, Zhuang JC, Zhou SY (2017) Induced earthquake sin the development of unconventional energy resources. *Sci China Earth Sci* 60. <https://doi.org/10.1007/s11430-017-9063-0>
- Yoon JS, Zang A, Stephansson O (2014) Numerical investigation on optimized stimulation of intact and naturally fractured deep geothermal reservoirs using hydro-mechanical coupled discrete particles joints model. *Geothermics* 52:165–184
- Zang A, Oye V, Jousset P, Deichmann N, Gritto R, McGarr A, Majer E, Bruhn D (2014) Analysis of induced seismicity in geothermal reservoirs – an overview. *Geothermics* 52:6–21
- Hazzard JF, Young RP (2002) Moment tensors and micromechanical models. *Tectonophysics* 356:181–197